Chapter 4

Magnetic field induced up-turn resistivity and low temperature carrier compensation in nodal line semimetal InBi

4.1 Introduction

The exotic band structure of topological materials has become an exciting field of inquiry nowadays due to the variety of electronic structures across different members of the family. *E.g.*, in the case of a topological insulator (TI), the surface has a non-trivial electronic structure protected by time reversal symmetry whereas the bulk has the usual trivial electronic structure[85]. The Dirac semi-metals, Weyl semi-metals, *etc.* have, on the contrary, non-trivial bulk electronic structure[86]. These semi-metals also possess nodal points in them which are the touching points of their valence and conduction bands in the momentum space. The nodal structures (*i.e.*, the loci of nodal points in momentum space) of different topological materials discovered so far are quite rich with some newly discovered compounds within the family showing more complex structures. Thus, we have either

a nodal line[30], nodal chain[28], nodal knot[87], nodal-link[88]–[90] or nodal-net[91], [92], *etc.* denoting the richness of the underlying phenomena among them.

Few of the recently discovered promising nodal line materials are ZrSiX (X= S, Se, Te)[93], [94], Ag_2S[95], AX_2 (A = Ca, Sr, Ba; X = Si, Ge, Sn).[96], Ca_3P_2[97], CaP_3[98], CaTe[99], CaAuAs[100], CaAgX (X = P, As)[101], IrF_4[28], Mg_3Bi_2[102], XB_2 (X = Ti, Zr)[103], $SrAs_3$[104], Co_2TiX (Si, Ge or Sn)[105], Ta_3X (X = Al, Ga, Sn, Pb)[106], X_2Y (X = Ca, Sr, Ba; Y = As, Sb, Bi)[107], $YCoC_2$[108], MnN[109] and YH_3[110] *etc*. As the number of electronic states at the nodes in a nodal line system is more than that for a nodal point system, these compounds display various novel properties like large spin Hall effect[111], long-range Coulomb interaction[112], and flat Landau level[113] *etc*. Quite interestingly, the effect of spin orbit coupling on its electronic structure is such that either the nodal line remains protected by some symmetry of the system like *e.g.* inversion symmetry, reflection symmetry, non-symmorphic symmetry, *etc.* or the nodal line gets destroyed by virtue of a gap formation resulting from the lack of such a protection[29], [30], [91], [114], [115]. For instance, the reflection symmetry of the Ta atomic plane protects the nodal line in XTaSe2 (X = Pb, Tl)[116], [117]. In the case of Cu3PdN, nodal lines are protected by the inversion symmetry[92]. For ZrSiS[93] and InBi[118] the nodal lines are protected by non-symmorphic symmetry. Although a vast amount of study has already been done on ZrSiS, InBi remains the least studied compound till date. InBi has two distinct nodal lines protected by non-symmorphic symmetry[118] and it also has a topologically non-trivial type-II Dirac cone protected by four-fold cyclic symmetry[118]. The compound InBi exhibits unique transport properties *viz.* extremely high magnetoresistance (XMR)[119], highly anisotropic MR[119] and pressure-induced superconductivity[120]. The compound also shows an upturn in the resistivity (ρ)[119] upon application of a magnetic field (**B**), but a detailed discussion on that topic is not available till date. The quantum oscillation study of this compound has also been reported earlier[121], but a deep understanding of its Fermi surface topology and its role in the transport phenomena is still lacking.

In this article, we report the structural, transport, electronic bandstructure and the Fermi

surface topology of InBi. The article is organized in the following way. We discussed the structural properties of InBi in Sec. 4.3.1. In Sec. **??**, we discuss its magnetotransport properties. In this section, we elaborated on an interesting result, *viz.* up-turn nature in $\rho(T)$. A detailed mathematical treatment is put forward to explain the observed temperature dependency of the resistivity. Another aspect of our study is establishing the role of electron and hole carriers in the transport phenomena. Our results further unravel the origin of XMR in InBi. In Chapter 5, We have discussed the Fermi surface topology by Shubnikov-de Haas (SdH) oscillations and compared it with the computed Fermi-surface using density functional theory (DFT). Our DFT result satisfactorily matches the experimental data. Accumulating the empirical and theoretical tools, we have successfully mapped the compound's Fermi surface. Such an inquiry gives a complete 3D visualization of its Fermi surface. We provide a detailed discussion for each Fermi surface sheet (FS). The modulation of each FS due to the electron and hole doping and the FS's role in the transport phenomena are also discussed rigorously. At the end, we have discussed about some important physical parameters derived from our SdH oscillation study.

4.2 Experimental details and theoretical methods

We prepared a single crystal of InBi using the modified Bridgman method. Elemental In (Alfa Aesar) and Te (Alfa Aesar), with 99.9% purity, have been used as the starting materials. The stoichiometric amount of starting materials were taken in an evacuated (10^{-6} mbar) quartz ampoule. The ingots were then melted at 200° C in the quartz ampoule and kept for 24 hrs at that temperature. The molten ingots were subsequently cooled to 150° C with a cooling rate of 20° hr^{-1}. Thereafter we cooled the molten material from 150° C to 30° C at a slow cooling rate of 3° hr^{-1}. As the bottom of the quartz tube is of a conical shape, the nucleation process starts from the bottommost point of the quartz tube. Shiny conical shaped single crystals are thus obtained from the quartz tube. Small parts of the crystal have been used for further characterization.

X-ray diffraction (XRD) of a powdered compound was performed for the structural anal-

ysis. Further, we also performed XRD on the compound's cleaved surface to check its single crystallinity. The XRD results from the cleaved surfaces identifies various crystallographic planes with respect to their Miller indices. Only reflections from planes of a certain Miller indices and their multiples were observed thus certifying the single crystallinity of the surface. The Hall study of the compound was performed on a rectangle-shaped sample with the four-point probe method in the van der Pauw configuration using a 9T Physical Property Measurement System (PPMS) and the Hall voltages were detected along the direction perpendicular to the current flow in the sample plane. The resistivity and the MR measurement was performed in the four probe puck in 15T Cryogen Free Magnet System (CFMS-15) from M/S cryogenic Ltd. UK. During MR and Hall measurements, the external magnetic field was applied perpendicular to the *ab*-plane.

in order to interpret our experimental results, we have carried out density functional theory calculations using full potential linearized augmented plane-wave based method implemented in the WIEN2k code[122]. All the calculations were performed in a non-spin polarized set-up with a generalized gradient approximation (GGA)[123] approach for the exchange-correlation functional. The spin-orbit coupling is included using a second-variational scheme and thus all the reported results are from GGA+SOC calculations. In order to obtain a very accurate Fermi energy (E_{F}), $R_{mt}K_{max}$ value is considered to be 7 and Brillouin zone (BZ) integration is done using tetrahedron method[124] with a sufficiently dense *k*-mesh ($14 \times 14 \times 14$).

4.3 Results and discussion

4.3.1 Structural characterization

We performed powder XRD in order to obtain the crystal structure of the compound. Our study suggests that the compound crystallizes in *p4/nmm* (Space group no. 129) crystal structure. The refinement of the powder XRD pattern yields a = 5.01(2) , b = 5.012(2) and c = 4.77(9) (A unit cell containing the In and Bi atoms is shown in FIG. 4.1 (a)). The plane containing In atoms are depicted by a shaded color. The BZ with its high symmetry

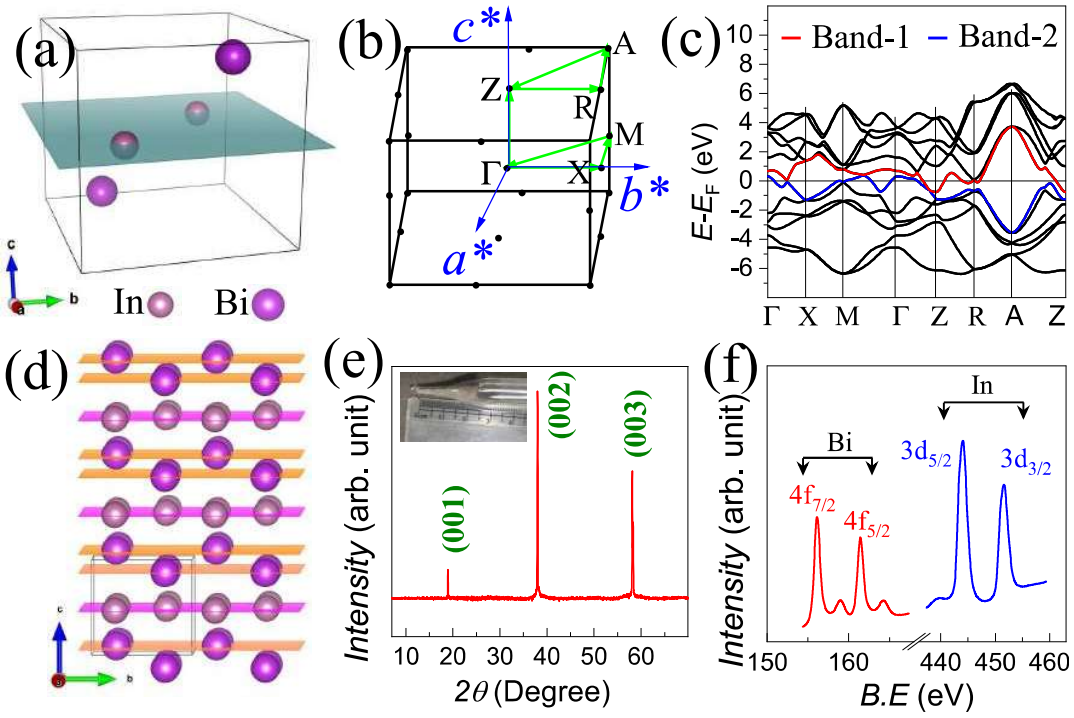

Figure 4.1: (a) The unit cell of InBi compound. (b) The BZ structure and the high symmetry points along which DFT calculation is performed. (c) The bandstructure along high symmetry points. The band-1 (red) and band-2 (blue) are only two bands that provide carriers' density at E_F. (d) The *ab*-planes of InBi. (e) The XRD peaks which originated from the *ab* plane. (Inset) The photograph of conical shape InBi single crystal. (f) The XPS spectrum of InBi

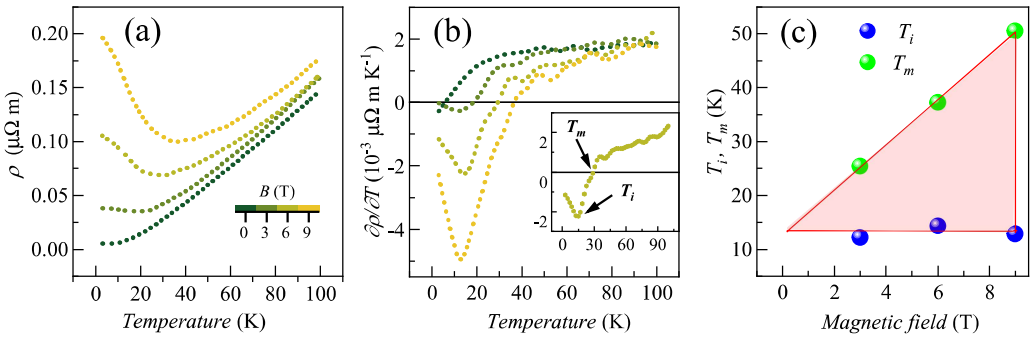

Figure 4.2: (a) $\rho(T)$ measured at 3–100 K with the application of 0–9 T magnetic field. (b)After performing $\frac{\partial\rho(T)}{\partial T}$ (to calculate turn-on temperature). The T_m and T_i are indicated in the inset figure. (c) The variation of T_m and T_i with the magnetic field. Triangle formed by T_m and T_i are shown by a pink shaded area.

points and the corresponding electronic bandstructure is shown in FIG. 4.1 (b) and (c). The bandstructure indicates that only two bands crossed the E_{F}. We label these two bands as band-1 and band-2 which are highlighted in red and blue color in FIG. 4.1 (c), respectively. The crystal structure of this compound is layered as shown in FIG. 4.1 (d) with the shaded planes indicating the occupancy of In and Bi atoms along the *ab*-planes. FIG. 4.1 (e) shows the XRD pattern taking from the *ab*-plane of the crystal. As the diffraction occurred only from the *ab*-planes, the diffractogram only contains $(00l)$ peaks. The very sharp peaks of the XRD pattern indicate the good crystallinity of the compound. The $(00l)$ peak pattern is also consistent with the space group and unit cell parameters derived from the powder XRD. We show the photograph of our conical-shaped single crystal along with a centimeter scale in the inset of FIG. 4.1 (e). The X-ray photoelectron spectroscopy (XPS) of InBi is shown FIG. 4.1 (f). The spectrum from $4f$ and $3d$ orbitals of Bi and In atoms well verified the compound's elemental composition. The XPS spectrum also agrees with the stoichiometry of the chemical composition.

4.3.2 Magnetic field dependent $\rho(T)$

The temperature dependent resistivity measured at 3–100 K is shown in FIG. 4.2 (a). The resistivity of the compound at 3 K and 100 K are 0.5×10^{-2} and 14.7 $\times10^{-2}$ $\mu\Omega$ m, respectively, which is very close to the earlier reported result[119]. To calculate the residual-resistance ratio (RRR) of our compound, we performed our resistivity study upto 300 K.

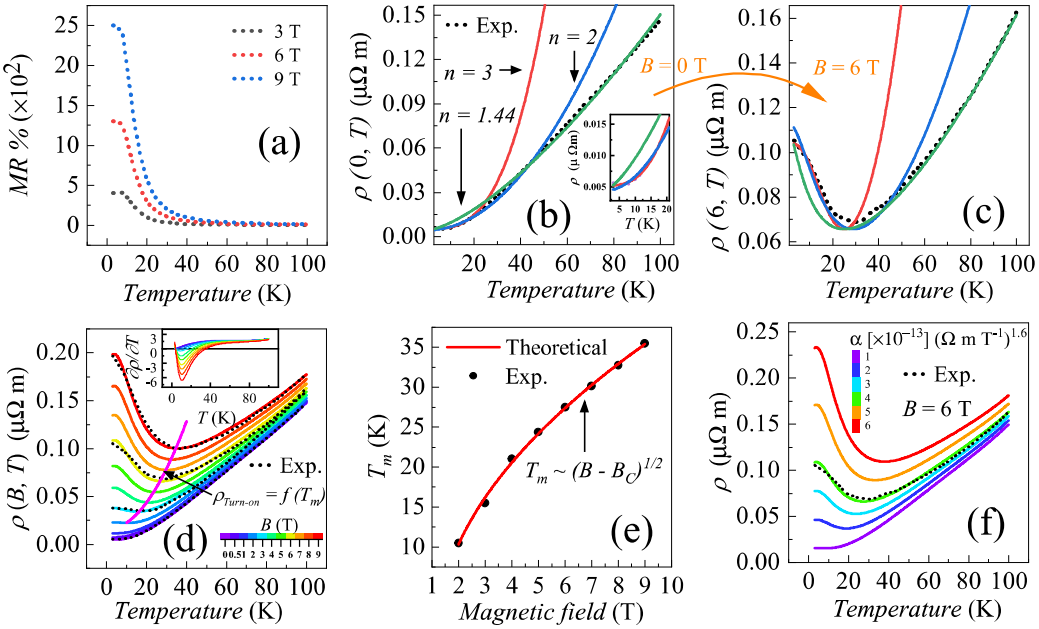

Figure 4.3: (a) Calculated $MR\%$ with the application of 3 T, 6 T and 9 T magnetic field. (b) Experimental $\rho(T)$ without any magnetic field and different type of fitted functions. Data upto 20 K is shown in the inset figure. (c) Experimental and simulated $\rho(T)$ with the application of the 6 T magnetic field. The colour code for the different *n* remain same as previous. (d) Simulated $\rho(T)$ under the application of 0–9 T magnetic field. Experimental $\rho(T)$ (shown as black dashed lines) are plotted over the theoretically generated one. The $\rho_{turn-on}$ as a function of T_m is indicated by a solid magenta line. The $\frac{\partial\rho(T)}{\partial T}$ of the theoretically generated patterns are shown in the inset figure. (e) Variation of turn-on temperature as a function of *B* and the fitted pattern. (f) Simulated $\rho(6, T)$ with the variation of α

.

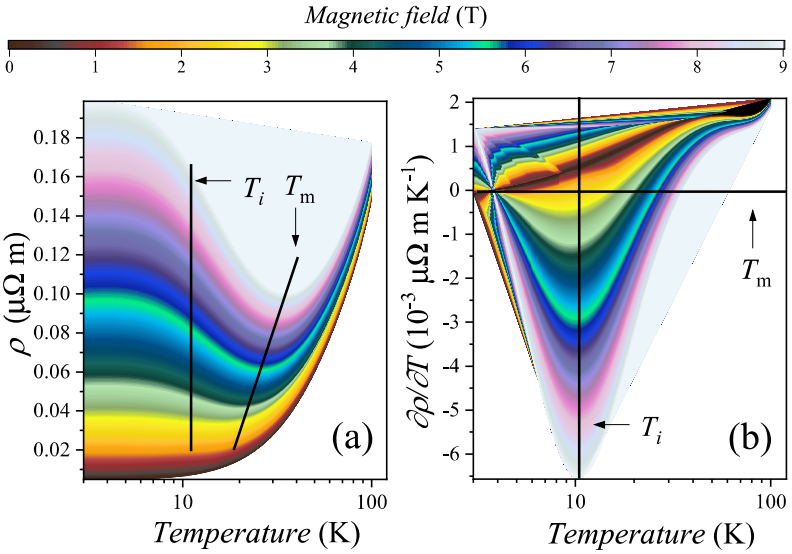

Figure 4.4: 3D contour plot of simulated data. (a) $\rho(B,T)$ (b) $\frac{\partial[\rho(B,T)]}{\partial T}$

The RRR of the compound based on the 3 and 300 K resistivity data is estimated to be 93. The RRR of the compound in the earlier reported data lies between 91-271[119]. We have observed that the resistivity of the compound sharply increases with the increase of magnetic field, especially in the low-temperature regime. Whene **B** = 0, resistivity of the compound have been increased monotonically with temperature. On applying the high magnetic field, the $\rho(T)$ rapidly decreases first, and then it increases with the increase of temperature. Such kind of up-turn behavior is also observed in other non-trivial topological systems[125]–[129], where applying certain magnetic field the $\rho(T)$ shows minima at a particular temperature (T_m).

We have shown the 1st order derivative $\frac{\partial[\rho(T)]}{\partial T}$ in FIG. 4.2 (b). Turn-on temperature is indicated in the figure as T_m, where the slope of the $\rho(T)$ changes its sign from negative to positive. Apart from turn-on behavior, we have also identified the minima of the $\frac{\partial[\rho(T)]}{\partial T}$, indicated as T_i in FIG. 4.2 (b). The T_i of the compound is approximately estimated as 12 K, and it changes negligibly with the change of applied magnetic field. We have plotted the variation of T_m and T_i with the applied magnetic field in FIG. 4.2 (c). The triangle formed by the T_m and T_i is one of the vital features observed in the compensated semimetals[130]. The value of the slope inside the shaded area of the triangle is negative, whereas the upper outside region of the triangle shows the positive slope. For the case

of graphite and bismuth, the triangular phase diagram can be explained by the inequality $\hbar/\tau \lesssim \hbar\omega_c \lesssim k_B T$, where τ is the electron-phonon scattering time and ω_c is the cyclotron frequency[131]. In clean semimetals with low carrier density $\tau^{-1} \ll k_B T/\hbar$, and hence, there exists a wide temperature-field range where XMR and turn-on like behavior in resistivity appear. On the other hand, large carrier density and strong impurity scattering limit the MR in conventional metals.

We have calculated the *T*-dependent MR from the $\rho(T)$ data. The MR of the compound defined as

$$MR = [\rho(B,T) - \rho(0,T)]/\rho(0,T) \tag{4.1}$$

here, $\rho(B,T)$ denoted the resistivity of the compound as a function of magnetic field (*B*) and temperature (*T*). The compound's $MR\%$ at 3-100 K is shown in FIG. 4.3 (a). The $MR\%$ of the compound is very high at low temperatures. It goes up to 2500% at 9 T. We have observed that $MR\%$ of the compound reduces drastically from 0 to 20 K and it almost becomes negligible above 40 K.

In order to analyze the temperature dependence of $\rho(0,T)$, we have fitted $\rho(0,T)$ with several functions [FIG. 4.3 (b)]. First, in order t o analyze the low temperature region, we have fitted $\rho(0,T)$ as $A + BT^n$ (where A and B are the constants) up to 20 K. The result from the best-fitted parameter gives n = 3. In the second step, we fixed n = 2, and fitted the $\rho(0,T)$ up to 20 K. However, the fitted data using n = 2 is not well-matched compared to the previous case. Lastly, we have fitted $\rho(0,T)$ in the whole temperature range, and the best-fitted parameter for that scenario gives n = 1.44. In the last case, the fitted data is well-matched in high temperature, but it does not fit well in low-temperature region. The observation of n = 3 for our case indicates the departure of pure electron dominated scattering. Generally, n = 2 is observed for pure electron-correlated dominated scattering[132]. Similar kinds of behaviors (n = 3) are also observed for other compensated semimetals *viz*., LaSbTe[133] and LaBi[134]. Semimetal LaSb (n = 4)[127], elemental yttrium[135] and transition-metal carbide[136] also shown interband electron-phonon scattering.

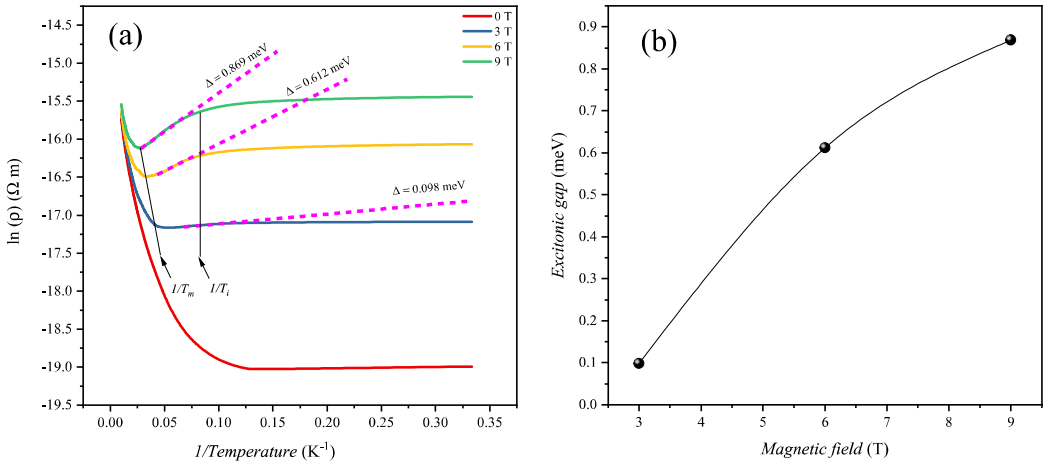

Figure 4.5: The calculation of excitonic gap. (a) The $\log(\rho)$ vs T^{-1} fiting, the slope of the particular regions ($T_i < T < T_m$) are shown by the dashed magenta line. (b) The variation of excitonic gap with the magnetic field.

4.3.3 Magnetic field dependent excitonic gap

We have calculated the excitonic gap which is generated by external magnetic field. We have calculated the insulating gap ($\triangle$) from the negative slope region of the field dependent $\rho(T)$. We have plotted the resistivity data as $\log(\rho)$ vs T^{-1} in the FIG. 4.5 (a). The regions $T_i < T < T_m$ where the slopes are calculated, have been indicated in the figure. The calculated slopes of the corresponding data are shown by the dashed magenta line. The derived insulating gap for the corresponding magnetic field is shown in FIG. 4.5 (b). The derived excitonic gap is lowest (0.098 meV) at 3 T, then it is increased at 6 T (0.612 meV) and 9 T (0.869 meV).

4.3.4 Origin of turn-on behavior

The MR of the compound based on the Kohler's law[137], [138] is defined as

$$MR = \alpha[B/\rho(0,T)]^m \tag{4.2}$$

Comparing the Eq. 4.1 and 4.2, we get

$$\rho(B,T) = (\alpha B^m/[\rho(0,T)]^{m-1}) + \rho(0,T) \tag{4.3}$$

Using Eq. 4.3, we have simulated the $\rho(T)$ under the 6 T magnetic field. During the simulation, we have fixed $\alpha = 1.2\times10^{-13}$ (Ω m T^{-1})$^{1.6}$ and $m = 1.6$, that are derived from the Kohler's law fitting (Eq. 4.2). Ideally, $m = 2$ for the perfectly compensated system but, our result $m = 1.6$ suggests that our compound slightly departs from the perfectly compensated case. The simulated patterns of $\rho(6,T)$ along with the experimental data are shown in FIG. 4.3 (c). Our study suggests that simulated $\rho(6,T)$, derived from the experimental $\rho(0,T)$ reasonably matches the experimental $\rho(6,T)$. we have also predicted $\rho(6,T)$ for all the corresponding cases of $\rho(0,T)$. Our simulated $\rho(6,T)$ in FIG. 4.3 (c) follows the same colour code for the corresponding cases of $\rho(0,T)$ in FIG. 4.3 (b). The result suggests that for $n = 3$ and 2, the theoretically generated $\rho(6,T)$ matches well at low temperature but deviates at high temperature. For the case of $n = 1.44$, simulated $\rho(6,T)$ fairly matches with experimental one at high temperature.

Using Eq. 4.3, we have simulated $\rho(B,T)$ for 0.5–9 T. We have plotted the theoretically generated $\rho(B,T)$ in FIG. 4.3 (d). The result matches the experimental data excellently. The experimental data are plotted as a black dashed line over the corresponding simulated pattern. Such an analysis validates our theoretical approach that replicates the experimental $\rho(B,T)$. We have also shown the first order derivative of $\rho(B,T)$ in the inset of FIG. 4.3 (d) in order to calculate the turn-on temperature (T_m). The derived T_m with the corresponding magnetic field are plotted in FIG. 4.3 (e). The variation of turn-on temperature with respect to the magnetic field is fitted with the equation

$$T_m = \zeta(B - B_c)^{\nu} \tag{4.4}$$

Such a formula was initially proposed D. V. Khveshchenko[139] and is validated for graphene and bismuth. For the graphite and bismuth the $\nu = 1/2$. The best fitted parameters in our case give $\zeta = 12.75$ K T$^{-0.5}$, $B_c = 1.36$ T and $\nu = 1/2$. $\nu = 1/2$ suggests that the turn-on nature of our compound follows the aforementioned picture.

The above theory suggests that the magnetic field opens an excitonic gap (in pyrolitic graphite) in the linear spectrum of the Coulomb interacting quasiparticles, and hence com-

pound shows semiconducting like transport feature. Further studies suggest that such kind of bandgap opening is not just limited to a particular compound rather it is observed across a wide range of compounds[127], [133]. One can calculate the semiconducting gap ($\triangle$) by $\log(\rho)$ vs T^{-1} fitting as $\rho(T) \propto \exp(\triangle/K_B T)$ within $T_i < T < T_m$ [127], [133]. Such a phenomena of a Coulomb-interaction driven electronic instability is found to occur in layered system possessing linear band dispersion at E_{F} under applied magnetic field [139]. Since our system too is layered and possesses linear band dispersions close to E_{F}, an excitonic gap could open up there, following the same phenomena. The excitonic gap for our compound at 3 T, 6 T and 9 T is 0.098 meV, 0.612 meV and 0.869 meV respectively. However, a saturation is observed in the resistivity at low temperatures which is ubiquitous in semiconductors[140] and other 2D metals[141], [142] . In our case too we have observed the saturation below T_i which does not also show any dependence on the excitonic gap or the applied magnetic field. It rather originates from those bands which are not gapped thus providing charge carriers for the conduction. These carriers are liable to get scattered by the impurities at low temperatures thus giving rise to the saturation.

In FIG. 4.3 (f), we simulate $\rho(B,T)$ with the variation of α. In the simulation, we fixed $B =$ 6 T, and observe how the variation of α affects the turn-on behavior. Our analysis suggests that lower the α higher the critical magnetic field needed to produce turn-on behavior. The analysis indicates that if $\alpha < 0.48\times10^{-13}$ (Ω m T^{-1})$^{1.6}$, we could not observe any turn-on behavior even at 6 T. The analysis highlights a significant role of α in the turn-on phenomena.

In this section, we provide a mathematical analysis for the turn-on behavior. We define a resistivity minima at T_m as $\rho_{turn-on}$. To calculate the minima in $\rho(B,T)$, we take $\frac{\partial[\rho(T,B)]}{\partial T}$ and make it zero at $T = T_m$. The mathematics is followed as

$$\frac{\partial[\rho(B,T)]}{\partial T}\Big|_{T=T_m} = 0 \tag{4.5}$$

Solving the Eq. 4.5, we get

$$\rho(0, T_m) = \alpha^{1/m}(m-1)^{1/m}B \tag{4.6}$$

To calculate the resistivity at turn-on temperature, we put $T = T_m$ in Eq. 4.3. The equation follows as:

$$\rho(B, T_m) = \alpha^{1/m}(m-1)^{1/m}\left(\frac{1}{m-1}+1\right)B \tag{4.7}$$

From Eq. 4.4, we already know that the parameter T_m is a explicit function of B. Hence, putting the value of B from Eq. 4.4 to Eq. 4.7, we get $\rho_{turn-on}$ as a function of T_m. After rewriting Eq. 4.7, we get

$$\rho_{turn-on}(T_m) = \alpha^{1/m}(m-1)^{1/m}\left(\frac{1}{m-1}+1\right)\left(\frac{T_m^2}{\zeta^2}+B_c\right) \tag{4.8}$$

Eq. 4.8 is valid for a particular compound that shows the similar kind of up-turn nature in $\rho(T)$ on the application of magnetic field. Putting the value of α = 1.2×10^{-13} (Ω m T^{-1})$^{1.6}$, m = 1.6, ζ = 12.75 K T$^{-0.5}$ and B$_c$ = 1.36 T, Eq. 4.8 in our case becomes

$$\rho_{turn-on}(T_m) = \left[\frac{T_m^2}{163}+1.36\right]\times 10^{-8} \tag{4.9}$$

We plot the Eq. 4.9 in FIG. 4.3 (d). The magenta line in the figure indicates the $\rho_{turn-on}$. The simulated $\rho_{turn-on}$ based on Eq. 4.9 excellently matches with the experimental results.

Based on the above analyses of the transport properties, we concluded the following: First, without the application of a magnetic field resistivity of the compound follows as A+BT^n. At low temperatures n = 3. But at high temperatures n becomes 1.44. Secondly, based on Eq. 4.3, we have generated a two dimensional data set (containing B and T) that fully replicates the experimental data. We have shown the simulated resistivity and its 1st derivative in a 3D contour plot in FIG. 4.4 (a) and (b). Thirdly, the parameter α has a significant role in producing the turn-on behavior in $\rho(T)$. Turn-on phenomena can

disappear if α becomes lower than a critical value. Finally, we can calculate the resistivity at the turn-on temperature (T_m) from our algebraic expression.

4.3.5 Step by step algebraic analysis of the resistivity up-turn

The MR of the compound is defined as

$$\boxed{MR = [\rho(B,T) - \rho(0,T)]/\rho(0,T)} \tag{4.10}$$

According to Kohler's law

$$\boxed{MR = \alpha[B/\rho(0,T)]^m} \tag{4.11}$$

From Eq. 4.10 and Eq. 4.11, we get

$$\implies [\rho(B,T) - \rho(0,T)]/\rho(0,T) = \alpha[B/\rho(0,T)]^m$$

$$\implies \rho(B,T) - \rho(0,T) = \alpha B^m \rho(0,T)^{1-m}$$

$$\boxed{\rho(B,T) = \alpha B^m \rho(0,T)^{1-m} + \rho(0,T)} \tag{4.12}$$

Eq. 4.12 expresses the resistivity as a function of magnetic field and temperature. So, if zero field $\rho(T)$ is known, one can generates a complete two dimensional data set of resistivity from Eq. 4.12 as it was discussed in SEC 4.3.4.

Role of α for generating resistivity minima: The right hand side of the Eq. 4.12 contains two terms. The first term is a 'decaying' term (for $m > 1$), whereas the second term is a 'growing' term. If the value of α becomes substantially low, the 'growing' term dominates and we can not get resistivity minima. If α increases, the 'decaying' term starts to dominate and, we get a critical value of α at where the turn-on nature begins to show. If α increases further, the 'decaying' term becomes stronger and hence, the decaying nature of

the resistivity follows up-to higher temperature. So, the higher the α, the higher the turn-on temperature. If α increases further, the whole resistivity pattern becomes decaying and we can not get any resistivity minima in the particular range of temperature. So role of α is crucial as it decide whether we get turn-on like behavior in the desired magnetic field and temperature range.

For the minima of the resistivity

$$\frac{\partial[\rho(B,T)]}{\partial T}\bigg|_{T=T_m} = 0$$

$$\implies \frac{\partial[\rho(B,T)]}{\partial T}\bigg|_{T=T_m} = \alpha B^m (1-m)\left[\rho(0,T_m)\right]^{-m} \cdot \frac{\partial[\rho(0,T_m)]}{\partial T} + \frac{\partial[\rho(0,T_m)]}{\partial T}$$

$$\implies \frac{\partial[\rho(0,T_m)]}{\partial T}\left[1 + \alpha B^m (1-m)\left[\rho(0,T_m)\right]^{-m}\right] = 0$$

In the above equation the term $\frac{\partial[\rho(0,T_m)]}{\partial T} = \frac{\partial[\rho(0,T)]}{\partial T}\Big|_{T=T_m} \neq 0$, so the remaining term would be:

$$\implies \left[1 + \alpha B^m (1-m)\left[\rho(0,T_m)\right]^{-m}\right] = 0$$

$$\implies \left[\alpha B^m (1-m)\left[\rho(0,T_m)\right]^{-m}\right] = -1$$

$$\implies \left[\rho(0,T_m)\right]^m = \alpha B^m (m-1)$$

$$\implies \boxed{\rho(0,T_m) = \alpha^{1/m} \cdot (m-1)^{1/m} \cdot B} \tag{4.13}$$

Now, putting $T = T_m$ in Eq. 4.12, we get

$$\rho(B,T_m) = \alpha B^m \rho(0,T_m)^{1-m} + \rho(0,T_m)$$

Putting the value of $\rho(B,T_m)$ (from Eq. 4.13) in the above equation, we get

$$\implies \rho(B,T_m) = \alpha B^m \left[\alpha^{1/m}(m-1)^{1/m}B\right]^{1-m} + \alpha^{1/m}(m-1)^{1/m}B$$

$$\implies \rho(B,T_m) = \alpha^{1/m}B(m-1)^{\frac{1-m}{m}} + \alpha^{1/m}B(m-1)^{1/m}$$

$$\implies \boxed{\rho(B,T_m) = \alpha^{1/m}\left[(m-1)^{\frac{1-m}{m}} + (m-1)^{1/m}\right]\cdot B} \tag{4.14}$$

The Eq. 4.14 suggests that resistivity at turn-on temperature proportional to magnetic field that is shown in the FIG. 4.2 (c). If the variation of turn-on temperature with respect to magnetic field is followed as:

$$T_m = \zeta(B - B_c)^{\nu} \tag{4.15}$$

Here critical magnetic field (B_c) and other constants *viz.*, ζ and ν in the equation are sample dependent parameters. The expression of B from Eq. 4.15 can be written as

$$\implies \left(\frac{T_m}{\zeta}\right)^{\frac{1}{\nu}} = B - B_c$$

$$\implies B = B_c + \left(\frac{T_m}{\zeta}\right)^{\frac{1}{\nu}} \tag{4.16}$$

Putting the value of B in Eq. 4.14, we get

$$\implies \boxed{\rho(T_m) = \alpha^{1/m}\left[(m-1)^{\frac{1-m}{m}} + (m-1)^{1/m}\right]\cdot\left[B_c + \left(\frac{T_m}{\zeta}\right)^{\frac{1}{\nu}}\right]} \tag{4.17}$$

This is a final equation which shows how turn-on resistivity varies with turn-on temperature. The Eq. 4.17 is shown by the magenta line of FIG. 4.3 (d).

4.3.6 Temperature dependent $\rho(B)$

The variation of $\rho(B)$ at several temperatures is shown in FIG. 4.6 (a). We have shown that the change of resistivity with temperature is very high when applied magnetic field is very

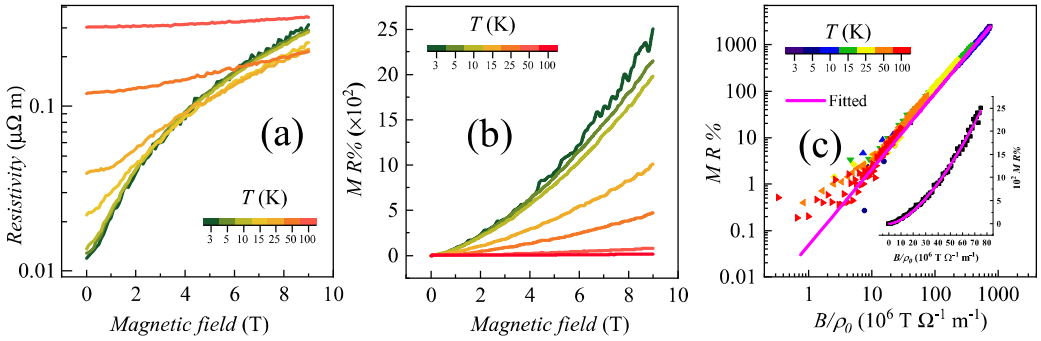

Figure 4.6: (a) The $\rho(B)$ measured at 3–100 K with the application of 0–9 T magnetic field. (b) The $MR\%$ as a function of *B* that is calculated from the experimental $\rho(B)$. (c) The log – log plot of $MR\%$ as a function of $B/\rho(0,T)$. The fitted line based on the Kohler's law is shown in a solid magenta line. The fitted line for 3 K is separately shown in the inset figure.

low and $\rho(B)$ for all temperatures tend to converge at high magnetic fields. It is observed that with the increase of *B*, $\rho(B,3)$ first grows and then it almost catches up the value of $\rho(B,15)$, $\rho(B,25)$ an $\rho(B,50)$ at 3 T, 4 T and 6 T respectively. The *MR%* as a function of *B* is shown in FIG. 4.6 (b). The *MR%* of the compound is very high large at 10 K and reaches up to 2500% at 3 K. On the other hand, *MR%* at high temperatures reduces drastically and almost becomes negligible above 25 K. We have also shown *MR% vs* $B/\rho(T,0)$ for all the temperatures in FIG. 4.6 (c). The log – log plot of all the data points falls in a single straight line. The fitted line based on the Eq. 4.2 is shown by a solid magenta line. During the fitting, we have put corresponding value of α and m as stated earlier. The fitted data at 3 K before the log – log plotting is shown in the inset of FIG. 4.6 (c). The falling of all data points in a straight line also verified our earlier assumption that the parameter α and m are almost temperature-insensitive in our compound.

4.3.7 Hall resistivity study

The Hall effect study in 0–9 T magnetic field at different temperatures are shown in FIG. 4.7. To eliminate the MR contribution from the Hall data, we performed the Hall study in the forward and reverse bias of the magnetic fields. As the MR does not change its sign while reversing the magnetic field unlike Hall resistivity, we subtract these two (data for forward and reverse bias) Hall data from each other and then divide them by two to get

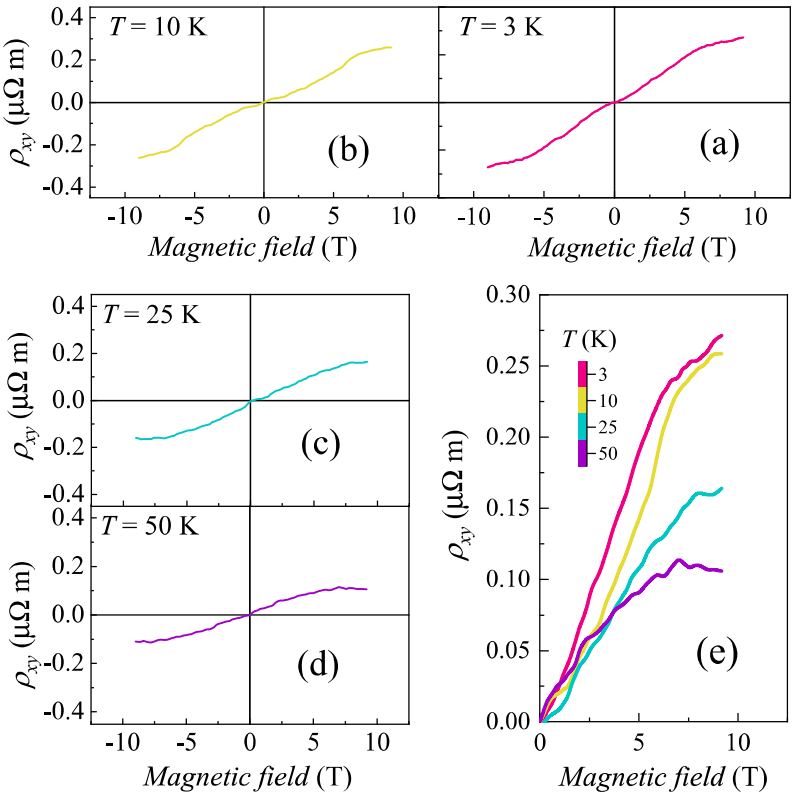

Figure 4.7: The $\rho_{xy}(B)$ from +9 T to -9 T at (a) 3 K, (b) 10 K, (c) 25 K and (d) 50 K. (e) The $\rho_{xy}(B)$ from 0–9 T with the temperature range 3–50 K

the actual Hall contribution. We followed the same process at 3 K, 10 K, 25 K, and 50 K in the full range of the magnetic fields. The non-linear behavior of the Hall resistivity suggests that both the carriers (electron and hole) contribute to the transport phenomena. The raw Hall data contained noise. The Hall data which are shown in the figure are plotted after smoothing the raw data. The whole set of the Hall data that are shown in FIG. 4.7 is reproducible, as we repeat the measurement using different pieces of single crystal along with the current variations. We have observed that at T $<$ 25 K, $\rho_{xy}(B)$ increases rapidly. On the application of 9 T magnetic field, ρ_{xy} at 3 K is almost twice compared to the ρ_{xy} at 25 K. Interestingly, the change in $MR\%$ calculated from ρ_{xx} also twice at the same temperature and magnetic field.

Using experimental result of $\rho_{xx}(B)$ and $\rho_{xy}(B)$, we have calculated the $\sigma_{xx}(B)$ and

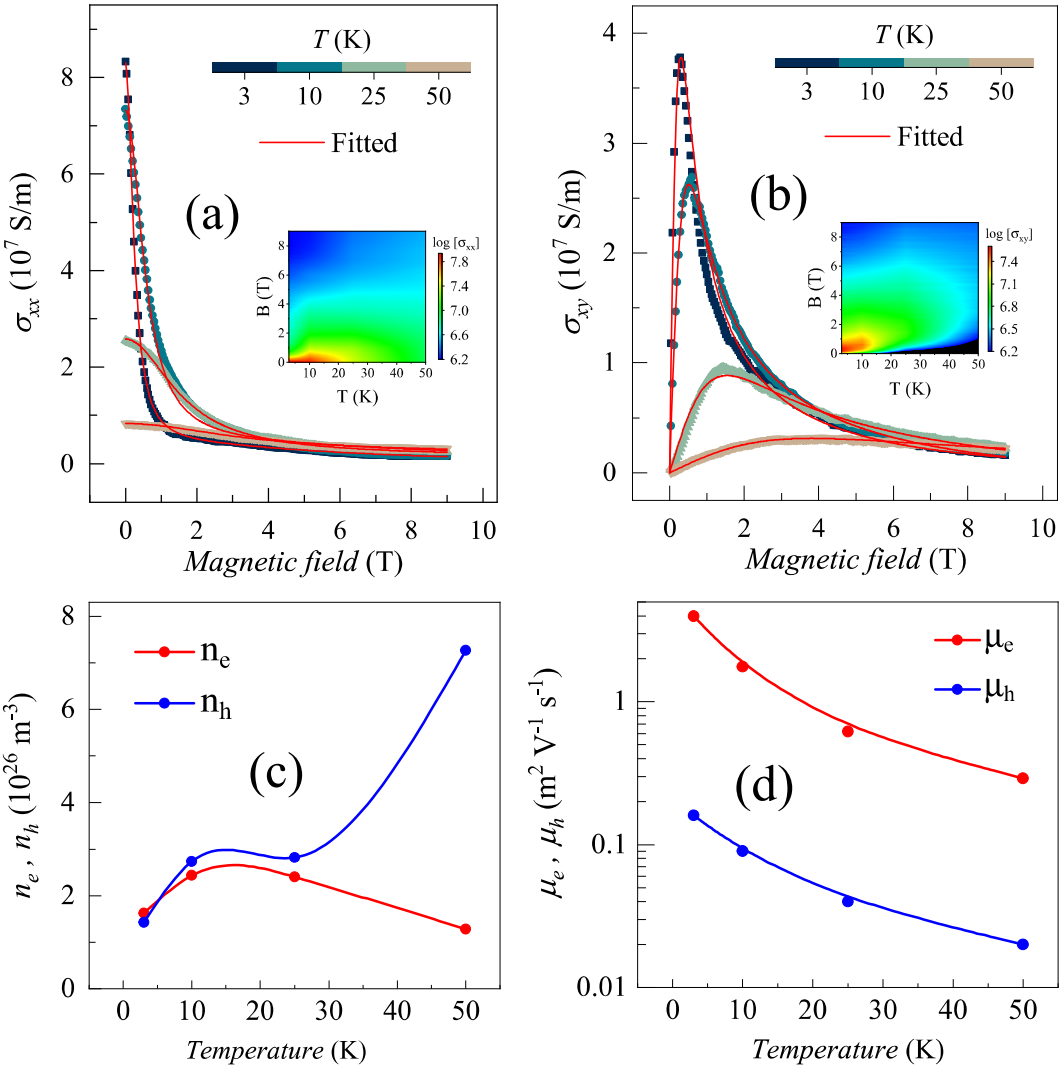

Figure 4.8: (a) $\sigma_{xx}(B)$ and its corresponding fittings, (inset) logarithmic plot of $\sigma_{xx}(B)$ as a function of magnetic field and temperature in a 3D contour plot. (b) $\sigma_{xy}(B)$ and its corresponding fittings, (inset) logarithmic plot of $\sigma_{xy}(B)$ as a function of magnetic field and temperature in a 3D contour plot. (c) The temperature-dependent electron and hole density which are estimated from the two carrier model. (d) The temperature-dependent electron and hole mobility which are estimated from the two carrier model.

$\sigma_{xy}(B)$. After the inverting of the resistivity matrix, $\sigma_{xx}(B)$ and $\sigma_{xy}(B)$ can be written as

$$\sigma_{xx}(B) = \frac{\rho_{xx}(B)}{[\rho_{xx}(B)]^2 + [\rho_{xy}(B)]^2} \tag{4.18}$$

$$\sigma_{xy}(B) = \frac{\rho_{xy}(B)}{[\rho_{xx}(B)]^2 + [\rho_{xy}(B)]^2} \tag{4.19}$$

Based on the Eq. 4.18 and 4.19, calculated $\sigma_{xx}(B)$ and $\sigma_{xy}(B)$ are plotted in FIG. 4.8 (a) and 4.8 (b).

We have fitted $\sigma_{xx}(B)$ and $\sigma_{xy}(B)$ with two band two carrier model[143] stated as

$$\sigma_{xx}(B) = e\left[n_h\mu_h\frac{1}{1+(\mu_h B)^2} + n_e\mu_e\frac{1}{1+(\mu_e B)^2}\right] \tag{4.20}$$

$$\sigma_{xy}(B) = eB\left[n_h\mu_h^2\frac{1}{1+(\mu_h B)^2} - n_e\mu_e^2\frac{1}{1+(\mu_e B)^2}\right] \tag{4.21}$$

As stated both the carrier types contribute to our transport phenomena, we have performed the global fitting based on the two carrier model where the simultaneous presence of the electron and hole carrier is considered. Here the electron density (n_e), the hole density (n_h), the electron mobility (μ_e) and the hole mobility (μ_h) are termed as fitting parameters. The fitted lines are shown as a solid red line in FIG. 4.8 (a) and (b). Extracted parameters from the Eq. 4.20 and 4.21 give almost the same result. The fitting parameters *viz*., $n_e(T)$, $n_h(T)$, $\mu_e(T)$, and $\mu_h(T)$ are shown in FIG. 4.8 (c) and (d).

From FIG. 4.8 (c), it is observed that $n_e(T)$ is slightly higher at 3 K but, as a broad view the $n_e(T)$ and $n_h(T)$ are approximately same ($\sim 1.5\times10^{-26}$ m^{-3}) below 25 K. After 25 K, $n_e(T)$ almost remains the same and $n_h(T)$ increases to $\sim 7\times10^{-26}$ m^{-3}. The results suggest that the number of electrons and holes contribute equally at lower temperatures whereas, at high temperatures, the transport is dominated by holes. Observing the MR data from FIG. 4.6 (b), we observed that MR% is also very large below 25 K. Such kind

of correlation hints that the XMR is accompanied by the electron-hole compensation of the compound. Regarding the carrier mobility, we have observed that the electron mobility of the compound at 3 and 15 K are 3.98 and 0.29 $m^2\ V^{-1}\ s^{-1}$ respectively. The hole mobility at 3 K and 15 K are 25 and 15 times lower than the corresponding electron mobility at that temperatures. The effective mobility ($\mu_{eff} \sim \sqrt{\mu_e \mu_h}$) at 3 K is 0.79 $m^2\ V^{-1}\ s^{-1}$ which is consistent with the previous report[119].

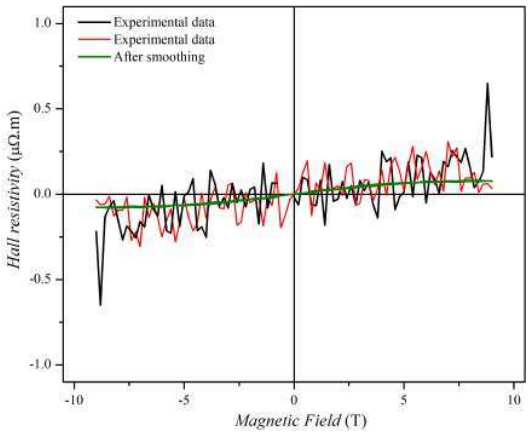

Figure 4.9: The Hall resistivity at 50 K. The experimental Hall data from +9 T→-9 T is indicated by the red line. The experimental Hall data from 0 T→+9 T and -9 T→0 T are indicated by the black line. The result (for the complete cycle of the magnetic field) after smoothing by adjacent averaging is shown by the green line.

4.3.8 The Hall resistivity at 50 K

We already know that a compound having both carriers (electron and hole) in transport does not always generate a smooth Hall data[144]. The data might fluctuate in the case of low carrier mobility. To get a smooth data, one can increase the current but that too is restricted by the Joule heating of the sample. We observed that the noise level is increased at high temperatures like 50 K and 100 K. **To get a lower noise level, we had performed the Hall experiment several times using different pieces of single crystal along with current variation, but noise does not vanished at 50 K and 100 K.**

We have smoothed the Hall data by 'adjacent averaging' methodology. The experimental data recorded at 50 K and the smoothed data are shown in FIG 4.9. The black and red lines denote the experimental Hall data while sweeping the magnetic field. The green line

indicates the smoothed data.

4.4 Conclusion

We presented a detailed discussion on transport phenomena of InBi. The turn-on phenomena of resistivity are intensely studied. We also present an in-depth analysis of the origin of turn-on behavior that justified our mathematical model. We have calculated the temperature-dependent carrier density and mobility for both carriers. We observed electron-hole carrier compensation follows up to 25 K. The high MR below 25 K indicates carrier compensation is one of the primary origins of the XMR. We also elaborated the origin of the observed metal-semiconductor transition by fusing the conventional Kohler's picture of MR in metals with some earlier findings. The magnetic field dependent T_m revealed that our system is likely to undergo a Coulomb interaction driven electronic instability. An excitonic band gap at the E_{F} was thus assumed to be opened by the application of a magnetic field in our case thus highlighting the electronic instability in the layers of the topological nodal line semi-metals under the action of magnetic field.